
EASYCHAUFFEUR: A BASELINE ADVANCING SIMPLICITY AND EFFICIENCY ON WAYMAX

A PREPRINT

Lingyu Xiao^{1,2*†}, Jiang-Jiang Liu^{2*}, Xiaoqing Ye², Wankou Yang^{1‡}, Jingdong Wang²

¹Southeast University ²Baidu

ABSTRACT

Recent advancements in deep-learning-based driving planners have primarily focused on elaborate network engineering, yielding limited improvements. This paper diverges from conventional approaches by exploring three fundamental yet underinvestigated aspects: training policy, data efficiency, and evaluation robustness. We introduce EasyChauffeur, a reproducible and effective planner for both imitation learning (IL) and reinforcement learning (RL) on Waymax, a GPU-accelerated simulator. Notably, our findings indicate that the incorporation of on-policy RL significantly boosts performance and data efficiency. To further enhance this efficiency, we propose SNE-Sampling, a novel method that selectively samples data from the encoder’s latent space, substantially improving EasyChauffeur’s performance with RL. Additionally, we identify a deficiency in current evaluation methods, which fail to accurately assess the robustness of different planners due to significant performance drops from minor changes in the ego vehicle’s initial state. In response, we propose Ego-Shifting, a new evaluation setting for assessing planners’ robustness. Our findings advocate for a shift from a primary focus on network architectures to adopting a holistic approach encompassing training strategies, data efficiency, and robust evaluation methods.

1 Introduction

The design of autonomous driving systems typically comprises three main components: prediction, perception, and planning. Recent advancements in deep learning techniques have greatly contributed to the progress of prediction tasks, revolutionising the onboard perception system. The planning module, which serves as the decision-making stage of the autonomous driving system, directly impacts overall performance and is rarely investigated in depth. One approach is to design the planning module along with the other two components in an end-to-end manner, meaning all modules are optimised jointly. However, this highly coupled design results in low explainability. Another approach is to design the planning module independently, known as the mid-to-end manner, where the perception module provides structured data to the planning module for generating control signals. In this paper, we focus on the latter approach.

In the realm of planning for autonomous driving, metrics are computed in both *close-loop* and *open-loop* settings. During *close-loop* evaluation, the ego vehicle’s states are computed via real-time interaction in the simulator, while in *open-loop*, they are merely replayed through predetermined logs. This characteristic has motivated previous methods to embrace Imitation Learning (IL), treating planning as a supervised regression task since *open-loop* emphasises the difference between prediction and replayed logs.

As the field of driving has matured, to improve performance in *close-loop*, most works have focused on network engineering by incorporating some degree of environmental interaction. Examples include combining rule-based planners with learning-based ones Dauner et al. [2023], introducing Monte-Carlo Tree Search (MCTS) in the decision-making phase Chekroun et al. [2023], or formulating the problem with hierarchical game theory Huang et al. [2023]. It is important to note that the accumulation of errors can significantly amplify over time steps during *close-loop* evaluation, necessitating the ability to prevent safety hazards. However, given that the collected demonstrations for IL primarily consist of flawless trajectories without any explicit instruction on avoiding accidents, the potential for

*Equal contribution. † Work done during an internship at Baidu. ‡ Corresponding author.

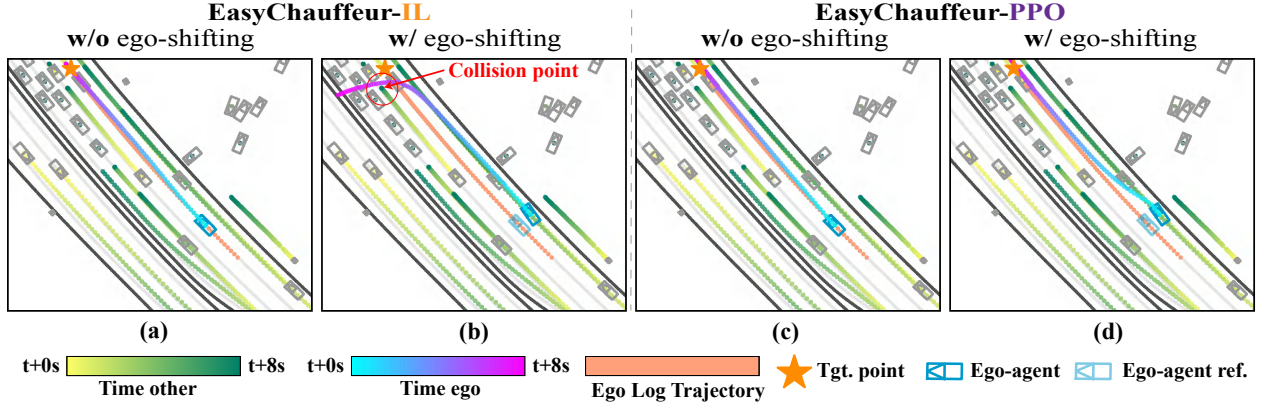


Figure 1: Comparison of the robustness of EasyChauffeur-IL and EasyChauffeur-PPO to the initial state under *close-loop* evaluation. ‘Tgt. point’ stands for the target point. ‘ego agent ref.’ refers to the initial state of the ego agent used as a reference when evaluated under Ego-Shifting. The current setting for evaluation may not fully assess the planners’ robustness, as shown in (a) and (c) where both models arrived successfully. However, when evaluated under Ego-Shifting, EasyChauffeur-IL (b) experiences a collision, while EasyChauffeur-PPO (d) demonstrates strong robustness. More visualisation results can be found on supplementary materials.

substantial improvements through intricate design is limited. On the other hand, even though Reinforcement Learning (RL) is inherently characterized by adequate interaction, none of the methods under this category, such as those referenced in Liu et al. [2022], Huang et al. [2022], Lu et al. [2023], demonstrate strong scalability, effectiveness, and high reproducibility on a standardized large-scale benchmark like nuPlan Caesar et al. [2021] due to time-consuming rollouts on CPUs. Although the recently released GPU-accelerated simulator Waymax Gulino et al. [2024], initialized with over 250 hours of real driving data from the Waymo Open Motion Dataset (WOMD) Ettinger et al. [2021], makes cost-effective large-scale training and evaluation possible, there is neither open-source training code available for the community to use, for IL or RL, nor a released model to compare with.

In this paper, to address the aforementioned problems, we conduct our study from three fundamental yet previously overlooked dimensions: training policy, data efficiency, and evaluation robustness. We begin by introducing a simple yet effective baseline planner for the community, applicable to both IL and RL. ‘Simple’ stands for straightforward design with all necessary components, while ‘effective’ denotes performance that is comparable to or better than the reported metrics in Gulino et al. [2024]. Surprisingly, we find that introducing an on-policy RL strategy, namely Proximal Policy Optimisation (PPO) Schulman et al. [2017], into planner training can greatly improve performance with only approximately 0.6% of the data.

Furthermore, with regard to data considerations, an ablation study on the volume of training data for IL reveals a phenomenon characterized by premature saturation with limited performance potential, suggesting that the data is redundant and easy to fit. Intuitively, we propose a sampling method called SNE-Sampling (Stochastic Neighbor Embedding-based Sampling), which operates on the latent space to select representative data. RL trained with data from SNE-Sampling has proven to have a significant performance gain compared to the vanilla approach.

Lastly, during *close-loop* evaluation, we find that performance in the simulator and the real-world is misaligned: the simulator lacks the imperfect initial localisation that is widely present in reality, for example, overtaking, pulling over, or localisation errors. The absence of such demonstrations in evaluations allows nearly perfect imitation to achieve good results instead of focusing on whether the model is robust enough to respond appropriately, as demonstrated in Fig. 1. Therefore, we rethink this sim-to-real gap by proposing an Ego-Shifting setting that can be integrated into any simulator. Experiments demonstrate that IL methods have much worse generalizability than PPO under this setting.

Most importantly, these interesting findings collectively highlight the potential shift from conventional network engineering approaches to the design of training strategies, the efficiency of data use, and the exploration of different evaluation directions.

The main contributions of this paper are summarised as follows:

- **Framework-wise:** We provide the community with a simple yet effective planner for IL and RL on the WOMD-driven Waymax.

- **Data-wise:** Extensive experiments prove that RL can be scalable with limited training data ($\sim 0.6\%$), and we propose SNE-Sampling to select representative training data.
- **Evaluation-wise:** To address the sim-to-real gap in *close-loop* evaluation that overlooks the assessment of models’ robustness, we propose an Ego-Shifting evaluation setting that can be applied to any simulator.

2 Related Work

2.1 Ego-Planning with Imitation Learning

End-to-End. The end-to-end planner aims to produce future trajectories directly from raw sensor input. A naive approach involves directly mapping control signals via a CNN Codevilla et al. [2018, 2019]. Later works have managed to fuse multimodal information by performing planning in BEV space Chitta et al. [2021] or by incorporating LiDAR and camera data Chitta et al. [2022], encoding the map with VectorNet Zhang et al. [2021a]. Other works closely integrate planning and perception. LAV Chen and Krähenbühl [2022] leverages additional information from other vehicles for better reasoning. STP3 Hu et al. [2022] perceives spatial-temporal features and plans a safe maneuver. VAD Jiang et al. [2023] injects every vectorized element into the transformer and supervises it with certain constraints. UniAD Hu et al. [2023a] utilises a systematic model design, connecting intermediate task nodes through query vectors and jointly optimising them. However, as all modules are highly coupled, future maintenance becomes challenging.

Mid-to-End. These approaches focus on generating control signals from post-perception results. For instance, PlanT Renz et al. [2023] utilised abstracted object-level representations for easy integration with existing perception algorithms. Unlike end-to-end planners, some works in this category have proven effective in real-world applications. SafetyNet Vitelli et al. [2022] incorporates a rule-based fallback layer to improve performance. UrbanDriver Scheel et al. [2022] was trained on a differentiable data-driven simulator built on perception outputs and high-fidelity HD maps from real-world data. SafetyPathNet Pini et al. [2023] selects a planning trajectory that minimises a cost considering safety and predicted probabilities. With the release of the first real-world large-scale standardised benchmark, nuPlan Caesar et al. [2021], recent works have conducted extensive studies using this benchmark. PDM Dauner et al. [2023] combined a rule-based planner with a learning-based approach, hotplan Hu et al. [2023b] utilised heatmap representation to predict future multimodal states, GameFormer Huang et al. [2023] treated interaction predictions as a game theory problem, and MBAPPE Chekroun et al. [2023] introduced MCTS in the decision-making phase. Additionally, Cheng et al. [2023] argues that *close-loop* and *open-loop* system evaluations are misaligned and proposes essential components for *close-loop* evaluation. However, all these IL-trained works may experience covariate shift and causal confusion.

2.2 Ego-Planning with Reinforcement Learning

Within the scope of end-to-end planners, CIRL Liang et al. [2018], built upon the Deep Deterministic Policy Gradient (DDPG) algorithm Lillicrap et al. [2015], was the first RL model applied to CARLA Dosovitskiy et al. [2017]. Inspired by this, Kendall et al. [2019] successfully employed DDPG in a real vehicle. To address the insufficiency of gradients obtained via RL, Toromanoff et al. [2020] successfully applied RL in CARLA when combined with IL. However, no reports have yet shown that RL outperforms IL in end-to-end planning Chen et al. [2023]. The situation changes when privileged information is available. Roach Zhang et al. [2021b] was trained using off-policy PPO with privileged BEV semantic segmentation, and the resulting dataset was used to train an IL agent, achieving superior performance. Isele et al. [2018] employed Deep Q-Network (DQN) with discretized BEV views to navigate a vehicle through intersections and occlusions. Wang et al. [2018] modified the Q-function network structure to accommodate a continuous action space for performing lane changes. While improvements have been achieved by Liu et al. [2022], Huang et al. [2022], Lu et al. [2023], and Isele et al. [2018], Wang et al. [2018], they have focused on specific scenarios or settings rather than conducting extensive evaluations on a large-scale benchmark.

3 Approach

3.1 EasyChauffeur

Network Design. The overall network structure is illustrated in Fig. 2. The design is straightforward and comprises three parts: Tokenisation, Transformer scene encoder, and MLP. The privileged information provided by the simulator (detection results when deployed in the real world) will be tokenised as a set of rectangles and fed into a transformer scene encoder separately by its own type. Since the input is one-dimensional and for simplicity, we utilise BERT Devlin et al. [2018] as the encoder. Here, a learnable embedding is introduced to fuse the privileged scene information via self-attention, thus serving as a latent space. After that, the fused feature is fed into an MLP that decodes the information

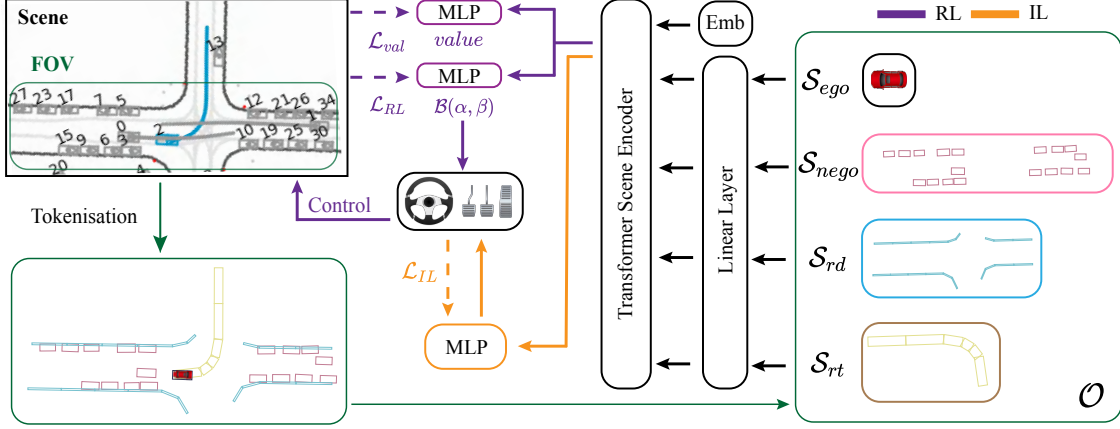


Figure 2: Overall pipeline of EasyChauffeur.

into actual control signals \mathcal{A} , e.g., steering and acceleration when using the bicycle action space, or the desired target point for the next timestamp when using the waypoints action space.

Input / Output Representation. The raw privileged scene information from Waymax is organised as follows: agents’ trajectories and properties (where agents are the collection of dynamic objects within a scenario, e.g., vehicles, pedestrians, bicyclists), road map, and routing for the ego agent. As described in Gulino et al. [2024], the routing is the union of expert log trajectories and drivable futures. However, WOMD does not release the drivable futures; we only use expert log trajectories as the ego agent’s routing. Next, we will introduce the tokenisation process for raw privileged information.

For static elements, the road map is represented as a set of dense points, as is the routing. The data format of dense points is redundant for our planner, since a set of dense points can be approximated through several control points Gao et al. [2020]. To reduce redundancy, we used the Ramer-Douglas-Peucker algorithm Ramer [1972], Douglas and Peucker [1973] to approximate the dense points into a set of sparse control points. A rectangle with a certain width and height is then extended based on the location of the sparse control points. Segments, namely, routing segments $\mathcal{S}_{rt} \in \mathbb{R}^{N_{rt} \times 6}$ and road edge segments $\mathcal{S}_{rd} \in \mathbb{R}^{N_{rd} \times 6}$, are the collections of rectangles for static road elements. N is the maximum number of rectangles within segments, and 6 attributes for each rectangle are $[x, y, w, h, yaw, id]$, where id is the sequential numerical index for that rectangle. The extended width for \mathcal{S}_{rt} and \mathcal{S}_{rd} is set to the ego agent’s width and $0.5m$ respectively.

For non-ego agents, we tokenised their properties into 6 attributes $\mathcal{S}_{nego} \in \mathbb{R}^{N_{nego} \times 6}$ similarly to the static ones, except we replace the id with $speed$ for each non-ego agent. For the ego agent $\mathcal{S}_{ego} \in \mathbb{R}^{1 \times 6}$, the attributes are aligned with \mathcal{S}_{nego} .

It should be noted that the tokenisation for \mathcal{S}_{rd} and \mathcal{S}_{veh} is only performed within the Field of View (FOV) under the ego agent coordinate system, with a certain width w_f and height h_f . After tokenisation, the stack for each segment is then represented as observation $\mathcal{O} = [\mathcal{S}_{rt}, \mathcal{S}_{rd}, \mathcal{S}_{nego}, \mathcal{S}_{ego}]$ for the planner. To distinguish each segment, we add an indicator to each one, thus, $\mathcal{O} \in \mathbb{R}^{(N_{rd} + N_{rt} + N_{nego} + 1) \times (6+1)}$.

The control signal \mathcal{A} from the MLP is determined by the action space: $\mathcal{A} \in \mathbb{R}^2$ (i.e., $[steer, acc]$) if we use the bicycle model and $\mathcal{A} \in \mathbb{R}^3$ for waypoints (i.e., $[x, y, yaw]$).

Training. The training scheme for IL and RL is presented in Fig. 2, highlighted by different colours. For IL, the network is directly supervised by the actions from the expert log,

$$\mathcal{L}_{IL} = \|\mathcal{A}_{gt} - \mathcal{A}\|_1. \quad (1)$$

$\|\cdot\|_1$ represents the l_1 norm. For RL, inspired by Zhang et al. [2021b], we use a Beta distribution to parameterise the continuous bicycle action space. We use PPO (Proximal Policy Optimization) with clipping to train the network. \mathcal{L}_{RL} is the clipped policy gradient loss with advantages estimated using Generalised Advantage Estimation Schulman et al. [2015]. \mathcal{L}_{value} is used to train the value network that is used to compute the advantage estimate,

$$\mathcal{L}_{value} = \|\mathcal{R} - value\|_2. \quad (2)$$

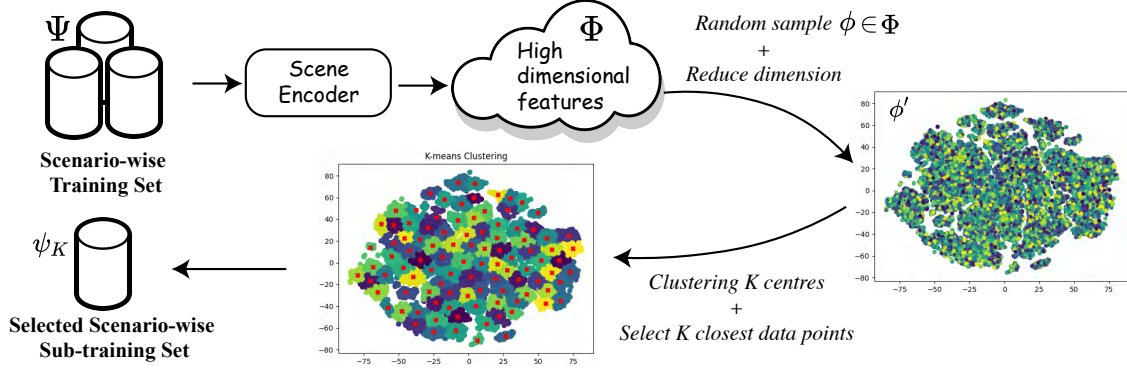


Figure 3: Illustration of SNE-Sampling. Scene encoder is pre-trained from EasyChauffeur.

\mathcal{R} is the reward provided by the simulator. The "value" is the output of the value network, and $\|\cdot\|_2$ represents the l_2 norm.

Reward Shaping. Building on the existing reward described in Gulino et al. [2024], the reward we used for RL consists of R_{speed} , $R_{offroad}$, $R_{wrongway}$, and $R_{collision}$. $R_{offroad}$ and $R_{collision}$ are consistent with the descriptions in Gulino et al. [2024]. The knowledge learned by the encoder from IL can be easily forgotten during RL iterations McCloskey and Cohen [1989]; therefore, we shape two additional rewards during the training process.

R_{speed} is a dense reward, representing the l_1 difference between the speed in the expert log and the actual speed during rollout.

$R_{wrongway}$ is a binary reward, judging whether the ego agent is driving the wrong way. A trajectory is considered to be the wrong way if:

- The difference between the current orientation angle of the ego agent and the orientation angle of the closest point on its expert log trajectory is larger than Δ_{yaw} .
- The Euclidean distance between the ego agent's current position and its nearest expert log trajectory point is greater than Δ_{dis} .

The final reward \mathcal{R} is the weighted sum of the rewards described above:

$$\mathcal{R} = w_s \times R_{speed} + w_o \times R_{offroad} + w_c \times R_{collision} + w_w \times R_{wrongway}. \quad (3)$$

3.2 Stochastic Neighbour Embedding Based Sampling

Motivation. Previous enhancements in the literature Dauner et al. [2023], Huang et al. [2023], Hu et al. [2023b] have predominantly focused on network design and complex engineering approaches. However, our research demonstrates the equally crucial role of data. Our study revealed that training EasyChauffeur with only 10% of the available training data in IL yielded performance comparable to using the full training set. This observation is in line with findings from Bronstein et al. [2023].

Furthermore, in the context of limited data, we made the surprising discovery that RL exhibits superior data efficiency compared to IL. With this insight, our goal was to design a sampling procedure that can extract a sufficiently representative subset for RL training.

Conventional random sampling techniques often assume a Gaussian distribution. While this assumption is reasonable if the entire training set follows a Gaussian distribution, it may not be optimal for better performance, as Gaussian distributions do not always represent the characteristics of neural networks well. Therefore, instead of this naive selection mechanism, we identify desired data points in the latent space of the networks.

Procedure. The aim of Stochastic Neighbour Embedding-based Sampling (SNE-Sampling) is to derive a representative subset containing K scenarios, denoted as $\psi_K \subset \Psi$, from the entire training set Ψ . The complete SNE-Sampling procedure is illustrated in Fig. 3.

We begin with the scenario-wise training set, passing it through a scene encoder trained using IL to produce a set of high-dimensional features, denoted as Φ . To reduce computational complexity, we initially sample a subset $\phi \subset \Phi$ at

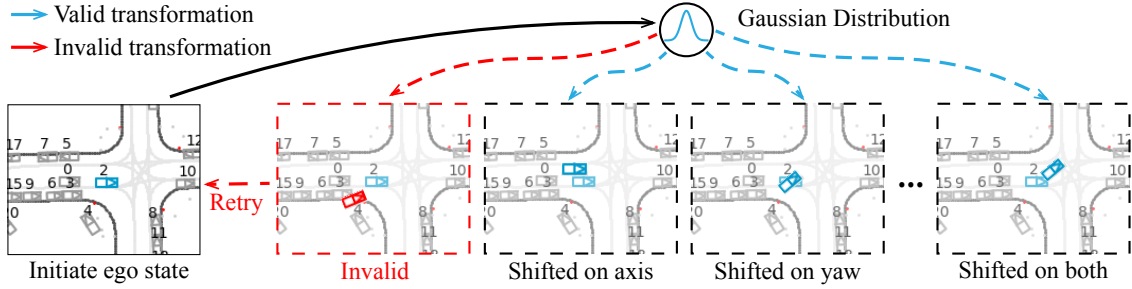


Figure 4: Diagram of Ego-Shifting. We perform a transformation on the ego agent on the x-y plane and the yaw axis; each transformed value is generated through a Gaussian distribution.

random, ensuring that the number of scenarios within ϕ is significantly larger than K . We then apply t-SNE Van der Maaten and Hinton [2008] to reduce the dimensionality of ϕ , resulting in ϕ' . Conceptually, a mapping function $f: \phi' \rightarrow \Psi$ exists such that each data point $p'_i \in \phi'$ can be associated with its corresponding origin in Ψ .

To extract the subset ψ_K , we perform k-means clustering on ϕ' to obtain K cluster centres. We then select the closest data point $p_i \in \phi'$ to each cluster centre and identify its corresponding mapping $f(p'_i) \in \Psi$. Consequently, the scenario-wise subset ψ_K comprises the collection of $(f(p'_1), \dots, f(p'_K))$.

3.3 Ego-Shifting for Robust Evaluation

Motivation. Conventional supervised learning operates under the assumption that the training and test set distributions are statistically similar. However, this assumption does not hold in real-world applications when the training set lacks diversity. This limitation is particularly pronounced in *close-loop* evaluation scenarios, as it is impractical to cover all possible routes from point A to B. Moreover, many *close-loop* benchmarks presuppose that the ego agent’s initial position is perfectly aligned, which fails to reflect real-world variances. In practice, ego agents may deviate from the intended route due to actions such as overtaking, pulling over, or imperfect localisation.

Procedure. Inspired by the above insight, we propose a novel evaluation perspective that can be applied to any existing *close-loop* evaluation protocol. The Ego-Shifting process is depicted in Fig. 4. The transformation process involves two aspects: geometric and coordinate transformations.

Geometrically, a maximum shifting value is defined for both the x-y plane and the yaw axis to regulate the transformation magnitude for each given initial ego state. The actual transformed values are generated using a Gaussian distribution. Validated transformations can occur along the axes (referred to as "shifted on axis"), along the yaw (referred to as "shifted on yaw"), or a combination of both (referred to as "shifted on both"). If a transformation is invalid, such as causing off-road incidents or collisions, we retry the process until the maximum number of retries is reached; otherwise, the initial state of the ego car is maintained.

Coordinate, all observations are shifted accordingly after the transformation is validated. In other words, we ensure that the observations are consistent with the ego agent’s coordinate system both before and after the transformation process.

4 Experiments

4.1 Evaluation Metrics & Settings

All experiments are conducted under *close-loop* evaluation following Gulino et al. [2024]. The descriptions of the evaluation metrics are listed below.

- **Off-road Rate (OR).** Off-road is a binary metric that describes whether a vehicle is on the road edge. A vehicle is considered off-road when overlap with the road edge is detected, and vice versa. 'Rate' refers to the percentage of episodes in which the metric is flagged at any timestep. The descriptions below are consistent.
- **Collision Rate (CR).** Collision is a binary metric that determines whether a vehicle is colliding with another object within the scene. When assessing each pair of objects, if their bounding boxes overlap in a top-down view in 2D during the same timestep, they are classified as being in collision.

Model	Training Policy	Action Space	Routing	AR \uparrow	OR \downarrow	CR \downarrow	PR* \uparrow
WF. Nayakanti et al. [2023]	-	Waypoints	LT+DF	-	7.89	10.68	123.58
WM. Gulino et al. [2024]	IL			-	4.14	5.83	79.58
Ours	IL	Waypoints	LT	85.96	2.80	2.93	95.77
WM. Gulino et al. [2024]	IL	Bicycle	LT+DF	-	13.59	11.20	137.11
	RL-DQN	Bicycle(discrete)		-	4.31	4.91	215.26
Ours	IL	Bicycle	LT	73.60	10.67	4.92	90.34
	RL-PPO			89.56	2.16	4.43	98.00

Table 1: Comparison with previous planning models presented on Waymax Gulino et al. [2024] (WM.) and adaptation from Wayformer Nayakanti et al. [2023] (WF). ‘LT’ and ‘DF’ under **Routing** shorts for Logged Trajectory and Drivable Futures (unavailable), respectively. We implement our method for continuous action space waypoints and bicycle. **PR***: it can not be compared directly for the unavailability of Drivable Futures. All evaluated under the **Reactive** setting.

- **Progress Ratio (PR)**. The progress ratio describes the percentage of the route that a vehicle has completed compared to the log trajectory. Since the future drivable area is not disclosed in WOMD, we exclude it from our calculation; therefore, the maximum value for PR for our method is 100.
- **Arrival Rate (AR)**. Arrival is a binary metric that determines whether a vehicle has arrived at the target point safely. A vehicle is considered to have arrived if it achieves more than a 90% progress ratio without collision or going off-road.
- **Non-reactive / Reactive**. Indicates whether non-ego agents are controlled by replayed logs or by IDM Treiber et al. [2000] during *close-loop* evaluation. The implementation of IDM directly follows Waymax.

4.2 Dataset

All the experiments are conducted on WOMD (v1.1.0). Results are reported on the validation split. The training of PPO and *close-loop* evaluation utilise recent released simulator Waymax Gulino et al. [2024], where data is also from WOMD. The sequence length for each scenario is 8 seconds recorded with 10 Hz, agents are controlled under the frequency of 10 Hz, maximum number of agents within a scenario is set to 128. Total scenario for training is 487,002 and 44,096 for validation. Since no drivable futures are provided by WOMD at this moment, the simulation will be terminated when ego agent considered arrive safely (description on **Evaluation Metrics & Settings** Arrival Rate part) during *close-loop* evaluation.

4.3 Implementation Details

Network Structure. For both RL and IL, we choose BERT-mini Bhargava et al. [2021] as transformer scene encoder. For IL, we use a 1-layer MLP with hidden dimension of 256. For RL we use a 2-layer MLP with hidden dimension of 64 for policy head and value head. To be notice that EasyChauffeur only generate control signal for next timestep rather than a sequence. This simplification is aimed at attenuating the impact caused by the model and emphasising the significant improvement brought about by changes in the training strategy.

Preprocessing for Observation. Ramer-Douglas-Peucker algorithm is used to sample dense points into sparse. The hyper-parameters for Ramer-Douglas-Peucker follow Renz et al. [2023] and can be found in supplemental materials. Instead of generating observation online during the training of IL, we will collect observation from 500 scenarios simultaneously and dump the concatenation of it for every simulated timesteps. Dynamic models to generate the ground truth control signal is aligned with the description on Gulino et al. [2024]. The observation has been transformed into ego coordinate system, thus only *speed* in \mathcal{S}_{ego} is a variance while others, namely, $[x, y, w, h, yaw]$ remain constant. For waypoints as action space, we do not fed ego agent since the *speed* deteriorates performance Cheng et al. [2023], while the determinate of acceleration at next state necessitates it’s current speed under bicycle model according to Newton’s laws of motion.

Hyperparameters. The width w_f and height h_f of FOV is set to 80m and 20m respectively. Threshold Δ_{yaw} and Δ_{dis} for $R_{wrongway}$ is set to 1 radians and 3.5m. Since all the weights on Eqn. 3 is binary except w_s is continuous, we intuitively set the binary one as -1.0 and continuous one as 1.0. We select 100, 400, 3,150 as K during SNE-Sampling and training for RL. Please refer to supplemental materials for detail setups and hyperparameters for IL and RL.

Training policy	Scenario number	Volume of training data	Non-reactive				Reactive			
			AR \uparrow	OR \downarrow	CR \downarrow	PR \uparrow	AR \uparrow	OR \downarrow	CR \downarrow	PR \uparrow
IL	100	$\sim 0.02\%$	50.24	19.53	24.62	78.18	52.22	19.16	8.50	78.57
	400	$\sim 0.08\%$	57.59	12.59	18.25	82.96	58.71	12.61	6.97	83.24
	3,150	$\sim 0.65\%$	60.19	15.73	16.02	86.04	61.69	15.81	8.40	86.29
	48,700	$\sim 10\%$	74.78	9.44	9.37	89.57	71.80	9.57	8.80	89.52
	487,001	100%	72.48	10.82	8.28	89.93	73.60	10.67	4.92	90.34
RL-PPO	100	$\sim 0.02\%$	84.38	5.84	6.41	97.72	83.87	5.91	5.82	97.79
	400	$\sim 0.08\%$	85.35	2.47	3.63	95.51	85.30	2.55	4.24	96.19
	3,150	$\sim 0.65\%$	86.76	1.91	3.11	94.53	86.29	1.94	3.69	95.01

Table 2: Ablation of the volume of training data for different training policies.

4.4 Effectiveness of EasyChauffeur

To demonstrate the efficacy of EasyChauffeur, in Tab. 4.2, we present comprehensive comparison with the results reported in Gulino et al. [2024]. Consistent with Gulino et al. [2024], we implement our method using action space waypoints (3rd row) and bicycle (6th row). In comparison to the methods reported in the literature (2nd and 4th rows), our method exhibits superior performance on metrics that can be fairly compared, such as Reactive-OR and Reactive-CR. These results establish the strength of our method as a pivotal reference point for further comparisons.

We do not implement our method under discrete action space for following reasons. First, the purpose of this paper is to provide a feasible & effective baseline, which has been proven under two different action space. Second, the detail for discretization under different action space is neither reported on Gulino et al. [2024], Nayakanti et al. [2023] nor within the scope of this paper, we leave this open for future researchers.

The selection of PPO over Deep Q-Network (DQN) in the Bicycle model is based on several primary considerations. Firstly, employing waypoint action space on Waymax is unrealistic due to the direct updating of the absolute position for the next simulated state. Consequently, not all transitions are kinematically compatible, and applying RL under waypoint action space may compromise physical constraints, leading to intricate reward shaping. Secondly, PPO supports both discrete and continuous action spaces. Furthermore, as our aim is to propose a baseline that is easy to reimplement, PPO generally exhibits better training stability compared to DQN. DQN is known to be sensitive to hyperparameter settings and can suffer from issues such as Q-value overestimation, which can impact training performance Van Hasselt et al. [2016]

4.5 Insights from Training with Limited Data

Tab. 4.5 presents the results of an ablation study on the volume of training data for various training strategies. The entire dataset is randomly sampled from the complete training set. Notably, an intriguing phenomenon emerges during the ablation study of IL: the network achieves comparable performance with only 10% of the data, as indicated by Non-reactive-AR and Reactive-AR. This premature saturation, accompanied by a low upper bound, suggests that the majority of driving scenarios are relatively simple to replicate, while challenging corner cases remain difficult to capture.

This observation is further supported by experiments involving the same network trained with the PPO strategy, as depicted in the last three rows of Tab. 4.5. Clear evidence indicates that the upper performance bound of the same network on the same data is significantly improved, although premature saturation persists. This finding suggests that some of the corner cases have been explored through numerous rollouts.

Based on these observations, we contend that instead of utilising the entire biased training set, selecting a representative subset has the potential to enhance performance. We chose 3,150 as the maximum number of scenario as this is the maximum number that our GPUs can perform rollout in parallel, which can be further engineeringly optimised.

4.6 Effectiveness of SNE-Sampling

The efficacy of our SNE-Sampling technique is showcased in Tab. 4.6, wherein the performance of various configurations is evaluated. Notably, all configurations exhibit enhancements in terms of AR, except for Non-reactive-AR, which shows a marginal degradation of -0.73 within acceptable limits. It is observed that as the magnitude of the scenario number escalates, the impact of SNE-Sampling becomes increasingly potent, manifesting in two discernible manners. Firstly, in comparison to random sampling, the augmentation in data volume yields greater performance improvements.

#Scenario	Non-reactive				Ractive			
	AR \uparrow	OR \downarrow	CR \downarrow	PR \uparrow	AR \uparrow	OR \downarrow	CR \downarrow	PR \uparrow
100	84.38	5.84	6.41	97.72	83.87	5.91	5.82	97.79
+SNE-Sampling	83.65 _(-0.73)	5.23	4.91	96.30	84.04 _(+0.17)	5.12	5.62	97.00
400	85.35	2.47	3.63	95.51	85.30	2.55	4.24	96.19
+SNE-Sampling	87.29 _(+1.94)	2.76	3.62	96.82	87.12 _(+1.82)	2.80	4.95	97.41
3,150	86.76	1.91	3.11	94.53	86.29	1.94	3.69	95.01
+SNE-Sampling	90.68 _(+3.92)	2.15	2.58	97.51	89.56 _(+3.27)	2.16	4.43	98.00

Table 3: Effectiveness of SNE-Sampling. AR under both Non-reactive and Ractive generally experience improvement for three different scenario number settings.

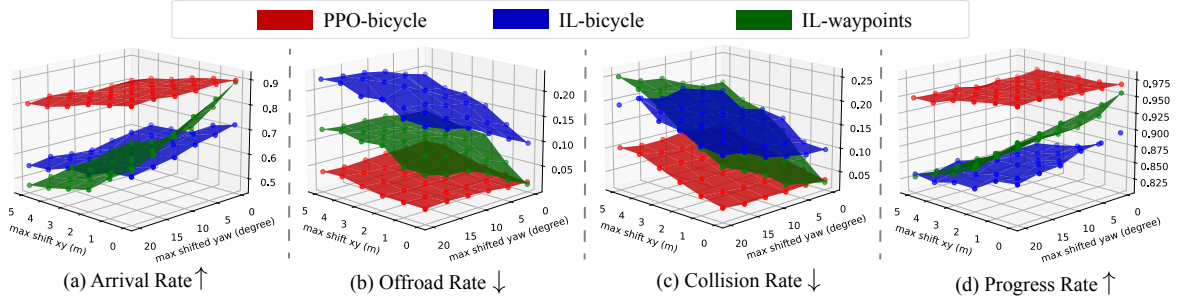


Figure 5: The performance of EasyChauffeur is evaluated under various training policies, Ego-Shifting properties, and action spaces.

Secondly, with each incremental increase in data volume, the advantage of SNE-Sampling over random sampling continues to expand.

4.7 Experiments on Ego-Shifting

Comparison under Different Ego-Shifting Properties. To enhance the efficiency of evaluation, we conducted an experiment on Ego-Shifting within a subset comprising 1050 scenarios involving Non-reactive agents. We specifically selected six steps based on the maximum values of shifted yaw and shifted xy, namely $[0, 4, 8, 15, 20]$ degrees and $[0, 1, 2, 3, 4, 5]$ meters, resulting in a total of 35 experiments. Subsequently, we plotted the trends of maximum shifting values against four evaluation metrics for EasyChauffeur, trained using PPO-bicycle, IL-bicycle, and IL-waypoints. The performance of EasyChauffeur under the aforementioned settings is depicted in Fig. 5.

Three key findings can be inferred from the results. Firstly, conventional IL methods exhibit significant variance in performance when the distribution of the validation set deviates from that of the training set. Notably, this variance increases as the degree of shifting intensifies. Secondly, positional changes are more sensitive to orientation angles. Illustratively, in the case of IL-waypoints (highlighted in green), the lowest arrival rate along the yaw axis (65.24%) is considerably higher than that along the xy axis (52.86%). Thirdly, even in the absence of any domain adaptation techniques, PPO-bicycle demonstrates superior long-term robustness compared to IL methods.

Analysis of Ego-Shifting. The concept of Ego-Shifting entails introducing out-of-distribution noise into a given distribution, thereby enabling the assessment of the anti-noise capabilities of different models. The visualisation of the feature distribution before and after performing Ego-Shifting for two models is presented in Fig. 6.

In the visualisation, the pink scattering denotes features belonging to the original data, while the light blue scattering represents the shifted data. The red and blue ‘X’ marks indicate the shifted centres for the data. Two degrees of shifting are visualised: LIGHT and HEAVY, corresponding to transformation pairs of (1m, 4 degrees) and (5m, 20 degrees), respectively.

Analysing the first row of Fig. 6, it becomes evident that the Ego-Shifting method proposed effectively alters the distribution of the validation set. As the application of LIGHT to the HEAVY transformation progresses from left to right, the distance between the non-shifted centre and the shifted centre increases, and the overlap area of two decrease. This observation serves as confirmation of the effectiveness of the proposed Ego-Shifting mechanism in modifying the distribution. Furthermore, the second row of Fig. 6 provides additional evidence highlighting the robustness of RL to

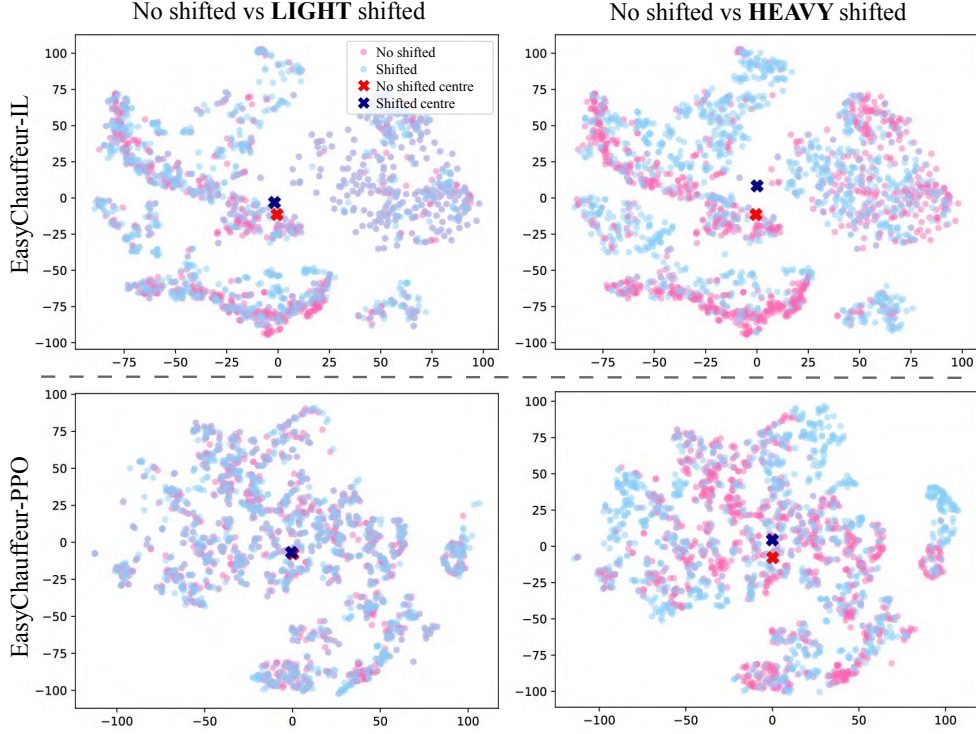


Figure 6: Visualisation of feature distribution before/after Ego-Shifting for EasyChauffeur-IL and EasyChauffeur-PPO.

environmental changes. Comparing the distances between the two centres and the overlap area of two clusters, it can be observed that the changes are minimal, indicating the ability of RL to adapt to the shifting environment.

5 Conclusion

In this paper, we illustrate that integrating reinforcement learning with minimal data can significantly enhance performance, facilitated by our novel SNE-Sampling technique. Furthermore, our Ego-Shifting evaluation method introduces a new perspective for *close-loop* evaluation, effectively reducing the sim-to-real gap. We advocate for a comprehensive strategy that balances innovative training, efficient data utilization, and rigorous evaluation to advance autonomous driving technologies.

References

- Daniel Dauner, Marcel Hallgarten, Andreas Geiger, and Kashyap Chitta. Parting with misconceptions about learning-based vehicle motion planning. In *Conference on Robot Learning (CoRL)*, 2023.
- Raphael Chekroun, Thomas Gilles, Marin Toromanoff, Sascha Hornauer, and Fabien Moutarde. Mbappe: Mcts-built-around prediction for planning explicitly. *arXiv preprint arXiv:2309.08452*, 2023.
- Zhiyu Huang, Haochen Liu, and Chen Lv. Gameformer: Game-theoretic modeling and learning of transformer-based interactive prediction and planning for autonomous driving. *arXiv preprint arXiv:2303.05760*, 2023.
- Haochen Liu, Zhiyu Huang, Jingda Wu, and Chen Lv. Improved deep reinforcement learning with expert demonstrations for urban autonomous driving. In *2022 IEEE Intelligent Vehicles Symposium (IV)*, pages 921–928. IEEE, 2022.
- Zhiyu Huang, Jingda Wu, and Chen Lv. Efficient deep reinforcement learning with imitative expert priors for autonomous driving. *IEEE Transactions on Neural Networks and Learning Systems*, 2022.
- Yiren Lu, Justin Fu, George Tucker, Xinlei Pan, Eli Bronstein, Rebecca Roelofs, Benjamin Sapp, Brandyn White, Aleksandra Faust, Shimon Whiteson, et al. Imitation is not enough: Robustifying imitation with reinforcement learning for challenging driving scenarios. In *2023 IEEE/RSJ International Conference on Intelligent Robots and Systems (IROS)*, pages 7553–7560. IEEE, 2023.

- Holger Caesar, Juraj Kabzan, Kok Seang Tan, Whye Kit Fong, Eric Wolff, Alex Lang, Luke Fletcher, Oscar Beijbom, and Sammy Omari. nuplan: A closed-loop ml-based planning benchmark for autonomous vehicles. *arXiv preprint arXiv:2106.11810*, 2021.
- Cole Gulino, Justin Fu, Wenjie Luo, George Tucker, Eli Bronstein, Yiren Lu, Jean Harb, Xinlei Pan, Yan Wang, Xiangyu Chen, et al. Waymax: An accelerated, data-driven simulator for large-scale autonomous driving research. *Advances in Neural Information Processing Systems*, 36, 2024.
- Scott Ettinger, Shuyang Cheng, Benjamin Caine, Chenxi Liu, Hang Zhao, Sabeek Pradhan, Yuning Chai, Ben Sapp, Charles R. Qi, Yin Zhou, Zoey Yang, Aur’elien Chouard, Pei Sun, Jiquan Ngiam, Vijay Vasudevan, Alexander McCauley, Jonathon Shlens, and Dragomir Anguelov. Large scale interactive motion forecasting for autonomous driving: The waymo open motion dataset. In *Proceedings of the IEEE/CVF International Conference on Computer Vision (ICCV)*, pages 9710–9719, October 2021.
- John Schulman, Filip Wolski, Prafulla Dhariwal, Alec Radford, and Oleg Klimov. Proximal policy optimization algorithms. *arXiv preprint arXiv:1707.06347*, 2017.
- Felipe Codevilla, Matthias Müller, Antonio López, Vladlen Koltun, and Alexey Dosovitskiy. End-to-end driving via conditional imitation learning. In *2018 IEEE international conference on robotics and automation (ICRA)*, pages 4693–4700. IEEE, 2018.
- Felipe Codevilla, Eder Santana, Antonio M López, and Adrien Gaidon. Exploring the limitations of behavior cloning for autonomous driving. In *Proceedings of the IEEE/CVF International Conference on Computer Vision*, pages 9329–9338, 2019.
- Kashyap Chitta, Aditya Prakash, and Andreas Geiger. Neat: Neural attention fields for end-to-end autonomous driving. In *Proceedings of the IEEE/CVF International Conference on Computer Vision*, pages 15793–15803, 2021.
- Kashyap Chitta, Aditya Prakash, Bernhard Jaeger, Zehao Yu, Katrin Renz, and Andreas Geiger. Transfuser: Imitation with transformer-based sensor fusion for autonomous driving. *IEEE Transactions on Pattern Analysis and Machine Intelligence*, 2022.
- Renrui Zhang, Rongyao Fang, Wei Zhang, Peng Gao, Kunchang Li, Jifeng Dai, Yu Qiao, and Hongsheng Li. Tip-adapter: Training-free clip-adapter for better vision-language modeling. *arXiv preprint arXiv:2111.03930*, 2021a.
- Dian Chen and Philipp Krähenbühl. Learning from all vehicles. In *Proceedings of the IEEE/CVF Conference on Computer Vision and Pattern Recognition*, pages 17222–17231, 2022.
- Shengchao Hu, Li Chen, Penghao Wu, Hongyang Li, Junchi Yan, and Dacheng Tao. St-p3: End-to-end vision-based autonomous driving via spatial-temporal feature learning. In *European Conference on Computer Vision*, pages 533–549. Springer, 2022.
- Bo Jiang, Shaoyu Chen, Qing Xu, Bencheng Liao, Jiajie Chen, Helong Zhou, Qian Zhang, Wenyu Liu, Chang Huang, and Xinggang Wang. Vad: Vectorized scene representation for efficient autonomous driving. *arXiv preprint arXiv:2303.12077*, 2023.
- Yihan Hu, Jiazhi Yang, Li Chen, Keyu Li, Chonghao Sima, Xizhou Zhu, Siqi Chai, Senyao Du, Tianwei Lin, Wenhui Wang, et al. Planning-oriented autonomous driving. In *Proceedings of the IEEE/CVF Conference on Computer Vision and Pattern Recognition*, pages 17853–17862, 2023a.
- Katrin Renz, Kashyap Chitta, Otniel-Bogdan Mercea, A Sophia Koepke, Zeynep Akata, and Andreas Geiger. Plant: Explainable planning transformers via object-level representations. In *Conference on Robot Learning*, pages 459–470. PMLR, 2023.
- Matt Vitelli, Yan Chang, Yawei Ye, Ana Ferreira, Maciej Wołczyk, Błażej Osiniński, Moritz Niendorf, Hugo Grimmer, Qiangui Huang, Ashesh Jain, et al. SafetyNet: Safe planning for real-world self-driving vehicles using machine-learned policies. In *2022 International Conference on Robotics and Automation (ICRA)*, pages 897–904. IEEE, 2022.
- Oliver Scheel, Luca Bergamini, Maciej Wołczyk, Błażej Osiniński, and Peter Ondruska. Urban driver: Learning to drive from real-world demonstrations using policy gradients. In *Conference on Robot Learning*, pages 718–728. PMLR, 2022.
- Stefano Pini, Christian S Perone, Aayush Ahuja, Ana Sofia Rufino Ferreira, Moritz Niendorf, and Sergey Zagoruyko. Safe real-world autonomous driving by learning to predict and plan with a mixture of experts. In *2023 IEEE International Conference on Robotics and Automation (ICRA)*, pages 10069–10075. IEEE, 2023.
- Yihan Hu, Kun Li, Pingyuan Liang, Jingyu Qian, Zhening Yang, Haichao Zhang, Wenxin Shao, Zhuangzhuang Ding, Wei Xu, and Qiang Liu. Imitation with spatial-temporal heatmap: 2nd place solution for nuplan challenge. *arXiv preprint arXiv:2306.15700*, 2023b.

- Jie Cheng, Yingbing Chen, Xiaodong Mei, Bowen Yang, Bo Li, and Ming Liu. Rethinking imitation-based planner for autonomous driving. *arXiv preprint arXiv:2309.10443*, 2023.
- Xiaodan Liang, Tairui Wang, Luona Yang, and Eric Xing. Cirl: Controllable imitative reinforcement learning for vision-based self-driving. In *Proceedings of the European conference on computer vision (ECCV)*, pages 584–599, 2018.
- Timothy P Lillicrap, Jonathan J Hunt, Alexander Pritzel, Nicolas Heess, Tom Erez, Yuval Tassa, David Silver, and Daan Wierstra. Continuous control with deep reinforcement learning. *arXiv preprint arXiv:1509.02971*, 2015.
- Alexey Dosovitskiy, German Ros, Felipe Codevilla, Antonio Lopez, and Vladlen Koltun. Carla: An open urban driving simulator. In *Conference on robot learning*, pages 1–16. PMLR, 2017.
- Alex Kendall, Jeffrey Hawke, David Janz, Przemyslaw Mazur, Daniele Reda, John-Mark Allen, Vinh-Dieu Lam, Alex Bewley, and Amar Shah. Learning to drive in a day. In *2019 International Conference on Robotics and Automation (ICRA)*, pages 8248–8254. IEEE, 2019.
- Marin Toromanoff, Emilie Wirbel, and Fabien Moutarde. End-to-end model-free reinforcement learning for urban driving using implicit affordances. In *Proceedings of the IEEE/CVF conference on computer vision and pattern recognition*, pages 7153–7162, 2020.
- Li Chen, Penghao Wu, Kashyap Chitta, Bernhard Jaeger, Andreas Geiger, and Hongyang Li. End-to-end autonomous driving: Challenges and frontiers. *arXiv preprint arXiv:2306.16927*, 2023.
- Zhejun Zhang, Alexander Liniger, Dengxin Dai, Fisher Yu, and Luc Van Gool. End-to-end urban driving by imitating a reinforcement learning coach. In *Proceedings of the IEEE/CVF international conference on computer vision*, pages 15222–15232, 2021b.
- David Isele, Reza Rahimi, Akansel Cosgun, Kaushik Subramanian, and Kikuo Fujimura. Navigating occluded intersections with autonomous vehicles using deep reinforcement learning. In *2018 IEEE international conference on robotics and automation (ICRA)*, pages 2034–2039. IEEE, 2018.
- Pin Wang, Ching-Yao Chan, and Arnaud de La Fortelle. A reinforcement learning based approach for automated lane change maneuvers. In *2018 IEEE Intelligent Vehicles Symposium (IV)*, pages 1379–1384. IEEE, 2018.
- Jacob Devlin, Ming-Wei Chang, Kenton Lee, and Kristina Toutanova. Bert: Pre-training of deep bidirectional transformers for language understanding. *arXiv preprint arXiv:1810.04805*, 2018.
- Jiyang Gao, Chen Sun, Hang Zhao, Yi Shen, Dragomir Anguelov, Congcong Li, and Cordelia Schmid. Vectornet: Encoding hd maps and agent dynamics from vectorized representation. In *Proceedings of the IEEE/CVF Conference on Computer Vision and Pattern Recognition*, pages 11525–11533, 2020.
- Urs Ramer. An iterative procedure for the polygonal approximation of plane curves. *Computer graphics and image processing*, 1(3):244–256, 1972.
- David H Douglas and Thomas K Peucker. Algorithms for the reduction of the number of points required to represent a digitized line or its caricature. *Cartographica: the international journal for geographic information and geovisualization*, 10(2):112–122, 1973.
- John Schulman, Philipp Moritz, Sergey Levine, Michael Jordan, and Pieter Abbeel. High-dimensional continuous control using generalized advantage estimation. *arXiv preprint arXiv:1506.02438*, 2015.
- Michael McCloskey and Neal J Cohen. Catastrophic interference in connectionist networks: The sequential learning problem. In *Psychology of learning and motivation*, volume 24, pages 109–165. Elsevier, 1989.
- Eli Bronstein, Sirish Srinivasan, Supratik Paul, Aman Sinha, Matthew O’Kelly, Payam Nikdel, and Shimon Whiteson. Embedding synthetic off-policy experience for autonomous driving via zero-shot curricula. In *Conference on Robot Learning*, pages 188–198. PMLR, 2023.
- Laurens Van der Maaten and Geoffrey Hinton. Visualizing data using t-sne. *Journal of machine learning research*, 9(11), 2008.
- Martin Treiber, Ansgar Hennecke, and Dirk Helbing. Congested traffic states in empirical observations and microscopic simulations. *Physical review E*, 62(2):1805, 2000.
- Nigamaa Nayakanti, Rami Al-Rfou, Aurick Zhou, Kratarth Goel, Khaled S Refaat, and Benjamin Sapp. Wayformer: Motion forecasting via simple & efficient attention networks. In *2023 IEEE International Conference on Robotics and Automation (ICRA)*, pages 2980–2987. IEEE, 2023.
- Prajwal Bhargava, Aleksandr Drozd, and Anna Rogers. Generalization in nli: Ways (not) to go beyond simple heuristics, 2021.
- Hado Van Hasselt, Arthur Guez, and David Silver. Deep reinforcement learning with double q-learning. In *Proceedings of the AAAI conference on artificial intelligence*, volume 30, 2016.

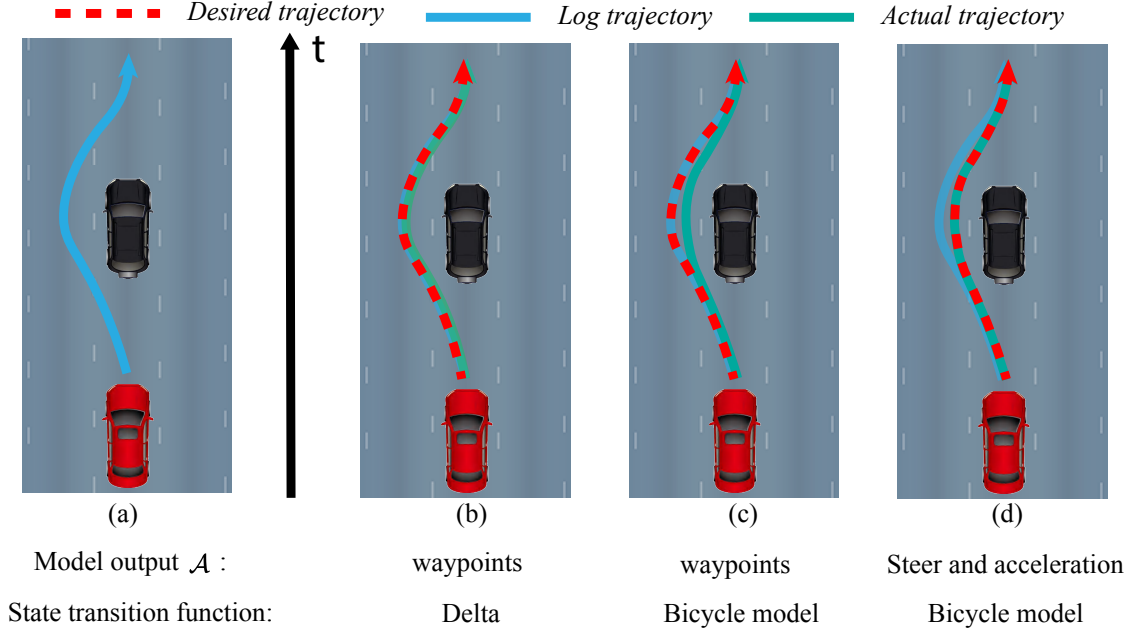


Figure 7: Illustration of different combinations of model output and state transition function.

A Videos

We provide videos on *close-loop* evaluation, located in a folder named `supp-demonstrations`². We categorise the videos by scenario into three sub-folders named `parkinglot`, `carriageways`, and `urban`. Within each sub-folder, you will find cases introduced in Figs. 9, 10, 11, and 12, named row-wise accordingly. For example, `1.mp4` refers to the first row in the figure. In addition to the mentioned cases, we provide more examples under `examples`. The file structure is organised as below:

```

supp-demonstrations
├── parkinglot
│   ├── examples
│   │   ├── ...
│   │   └── 1.mp4
│   └── ...
└── ...

```

B Dynamic Model

Waymax Gulino et al. [2024] provided two types of transition function to calculate agents’ next state: ‘Delta’ and ‘Bicycle model’. For ‘Delta’ state transition function, the transition from t to $t + 1$ is directly determined by the next state’s coordinate that fed into simulator, regardless it’s kinematics feasibility, thus ‘Delta’ may not consistent with reality application (may occurs teleport or spin in this case). On the other hand, for ‘Bicycle model’ as transition function, the simulator will calculate agents’ next state by steer and acceleration, which ensure that every state transitions are satisfy kinetic constraints.

Different combinations of model output \mathcal{A} and state transition function are demonstrated in Fig. 7. The desired trajectory is the trajectory that calculated by the set of model’s output. As Fig. 7(b) shows, there can be a gap between desired trajectory and actual trajectory if the action provided by model is not aligned with the state transition function, since a set of waypoints need to first fit by steer and acceleration before transited (also discussed on Cheng et al. [2023]). Thus, when referring waypoints as action space we use combination on Fig. 7(a) and bicycle as Fig. 7(c).

Waypoints. In this case, the model’s output is $\mathcal{A} = (\Delta x, \Delta y, \Delta yaw)$. Given the current agent’s state (x, y, yaw, v_x, v_y) , the next state $(x', y', yaw', v'_x, v'_y)$ is updated as:

²Download link: <https://drive.google.com/drive/folders/1LpAeBZJzXb7SrgqOfTY9KC6DJY6XjajD>

Parameters	Dynamic Model	
	bicycle	waypoints
learning rate	1×10^{-4}	
decay schedule	None	
optimiser	Adam	
epochs	5	
scenarios per-batch	500	
batch size	6	
$w_{acc} \setminus w_x$	1	
$w_{steer} \setminus w_y \ \& \ w_{yaw}$	5	50

Table 4: Hyperparameters for IL. Batch size and learning rate are reported for per-GPU.

$$\begin{aligned}
x' &= x + \Delta x \\
y' &= y + \Delta y \\
yaw' &= yaw + \Delta yaw \\
v'_x &= (x' - x) \cdot f \\
v'_y &= (y' - y) \cdot f.
\end{aligned} \tag{4}$$

f is the control frequency, which is 10Hz as mentioned in the paper. v_x and v_y is the velocity along x-axis and y-axis.

Bicycle. In this case, the model’s output is $\mathcal{A} = (a, s)$, a and s are acceleration and steer for the agent, respectively. Next state is updated according to:

$$\begin{aligned}
x' &= x + \frac{v_x}{f} + \frac{a \cdot \cos(yaw)}{2f^2} \\
y' &= y + \frac{v_y}{f} + \frac{a \cdot \sin(yaw)}{2f^2} \\
yaw' &= yaw + s \cdot \left(\frac{\sqrt{v_x^2 + v_y^2}}{f} + \frac{a}{2f^2} \right) \\
v' &= \sqrt{v_x^2 + v_y^2} + a/f \\
v'_x &= v' \cdot \cos(yaw) \\
v'_y &= v' \cdot \sin(yaw).
\end{aligned} \tag{5}$$

C Additional Hyperparameters

Imitation Learning. All experiments are conducted on 8 NVIDIA A800 GPUs. Since $\mathcal{A}_{gt} \in \mathbf{R}^n$, where n is the dimension of action space, Eqn. 1 should be expressed as:

$$\mathcal{L}_{IL} = w_{acc} \|a_{gt} - a\|_1 + w_{steer} \|s_{gt} - s\|_1, \tag{6}$$

for bicycle as dynamic model, or

$$\mathcal{L}_{IL} = w_x \|\Delta x_{gt} - \Delta x\|_1 + w_y \|\Delta y_{gt} - \Delta y\|_1 + w_{yaw} \|\Delta yaw_{gt} - \Delta yaw\|_1, \tag{7}$$

for waypoints as dynamic model.

Proximal Policy Optimization. The implementation of PPO is based on stable-baseline3³. Practically, we follow Zhang et al. [2021b] to introduce an entropy loss \mathcal{L}_{ent} to encourage exploration. Therefore the objective for PPO can be expressed as:

$$\mathcal{L}_{ppo} = \mathcal{L}_{RL} + w_{ent} \mathcal{L}_{ent} + w_{value} \mathcal{L}_{value}. \tag{8}$$

During evaluation, we take the mean of Beta distribution \mathcal{B} as the deterministic output.

³<https://github.com/DLR-RM/stable-baselines3>

Rollout			
rollout scenarios K	100	400	3,150
rollout GPUs	1	2	7
total timesteps	6M	16M	25M
action range ($acc/steer$)	[-6, 6]/[-0.3, 0.3]		
Training			
learning rate	3×10^{-4}		
epochs	1		
optimiser	Adam		
batch size	2,500		
scenarios per-batch	1		
γ for GAE	0.99		
λ for GAE	0.9		
max norm gradient clipping	0.5		
clipping range for PPO	0.2		
decay schedule	None		
w_{ent}, w_{value}	1, 0.01		
w_s, w_o, w_c, w_w	1, -1, -1, -1		

Table 5: Hyperparameters for PPO. We only use 1 GPU to update model’s weights. The ‘epochs’ under **Training** means the times to iterate all collected data from rollout.

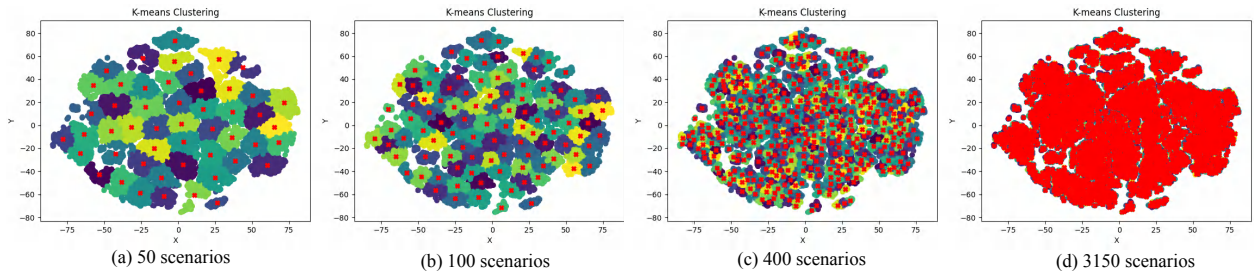


Figure 8: Visualisation of clustering centre (highlighted in red mark) for different K .

D Visualisation of SNE-Sampling

Fig. 8 illustrates the clustering centre under different settings of K , the number of scenarios. It is evident that with an increase in K from 50 to 3,150, the coverage rate of the red mark becomes comprehensive. When selecting 100 scenarios, the selected data are not sufficiently representative to observe a performance gain. However, with 400 scenarios, the improvement can be immediately highlighted.

E Visualisation Results Across Varied Scenarios

We illustrate some representative *close-loop* evaluation visualisations across different driving scenarios in Figs. 9, 10, 11, and 12. Vertically, we divide each driving scenario into two parts based on the curvature of routing: straight and curvy. Horizontally, we compare the performances of EasyChauffeur-IL and EasyChauffeur-PPO. Additionally, we provide visualisations with Ego-Shifting, referring to ‘w/ ego-shifting’, for comprehensive comparison on each scenario. Fig. 9 delves into parking lot scenario, detailing the navigation through congestion, pedestrian yielding, exiting into traffic, and executing minor-angle turns in tight spaces. Fig. 10 and 11 focus on dual carriageways, presenting high-speed travel on straight roads amidst traffic, followed by navigating curvaceous and narrow motorway sections, and exiting via slip roads. Fig. 12 explores urban driving, depicting straight routes into controlled intersections and roundabouts, manoeuvring a T-junction into a residential area, and turning at complex intersections with adjacent waiting vehicles. It can be seen that IL-trained planner performs well on easy scenarios and fails to tackle the complex ones, while the RL-trained planner presenting superior capability on various driving settings and scenarios.

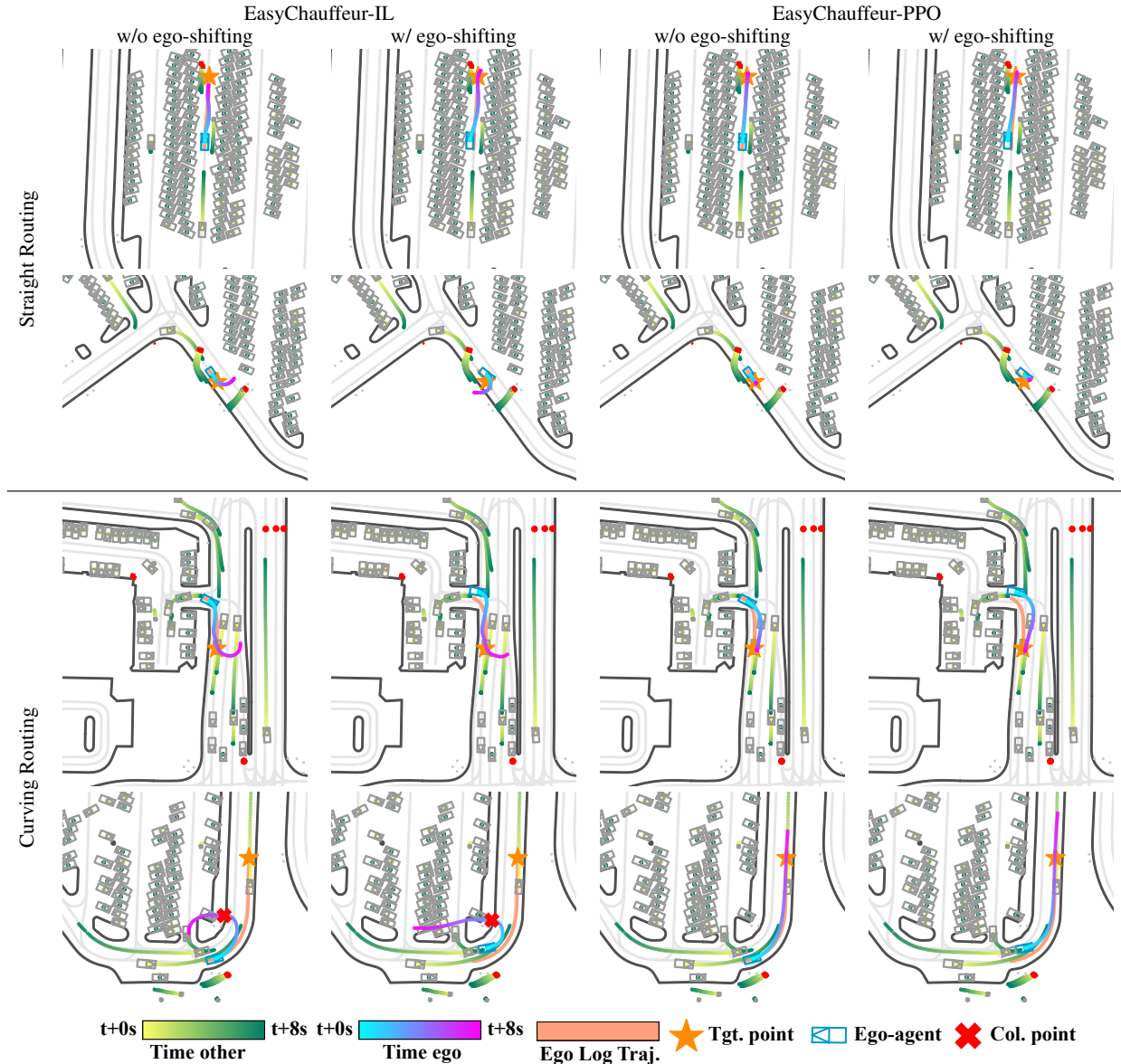


Figure 9: Visualisation of *close-loop* evaluation on parking lot. The initial scenario elucidates the process of navigating through a congested parking area. The subsequent scenario depicts the ego-agent advancing at a reduced pace, adhering to the requirement to yield to pedestrians. The third scenario illustrates the act of exiting the parking lot and integrating into a congested stream of traffic, ultimately halting due to traffic congestion. The final scenario demonstrates manoeuvring through a minor-angle turn within the confines of a narrow and congested parking area.

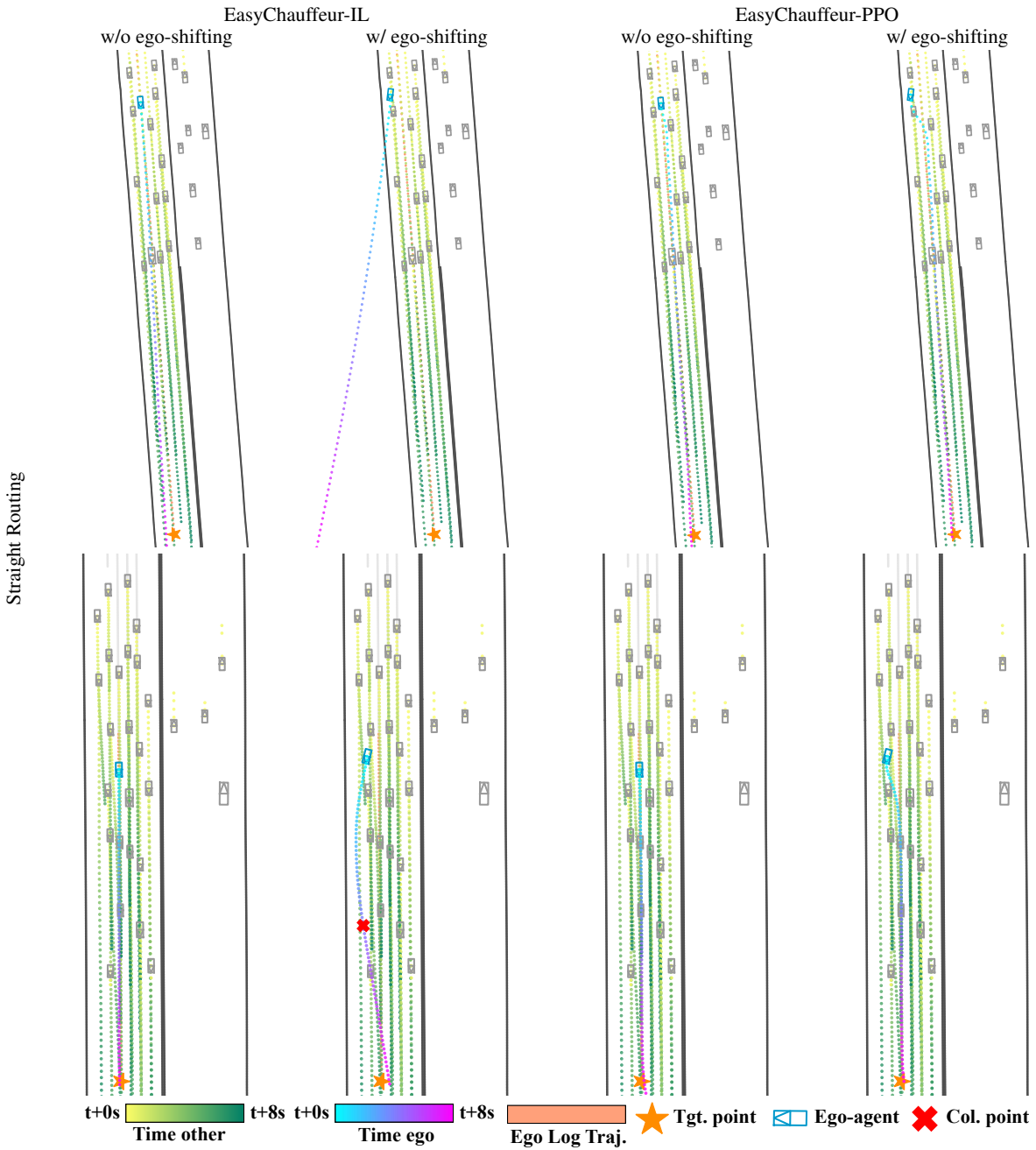


Figure 10: Visualisation of *close-loop* evaluation on dual carriageways. The two scenarios depict scenarios of high-speed traversal along complex, straight roads, characterised by the presence of numerous surrounding vehicles.

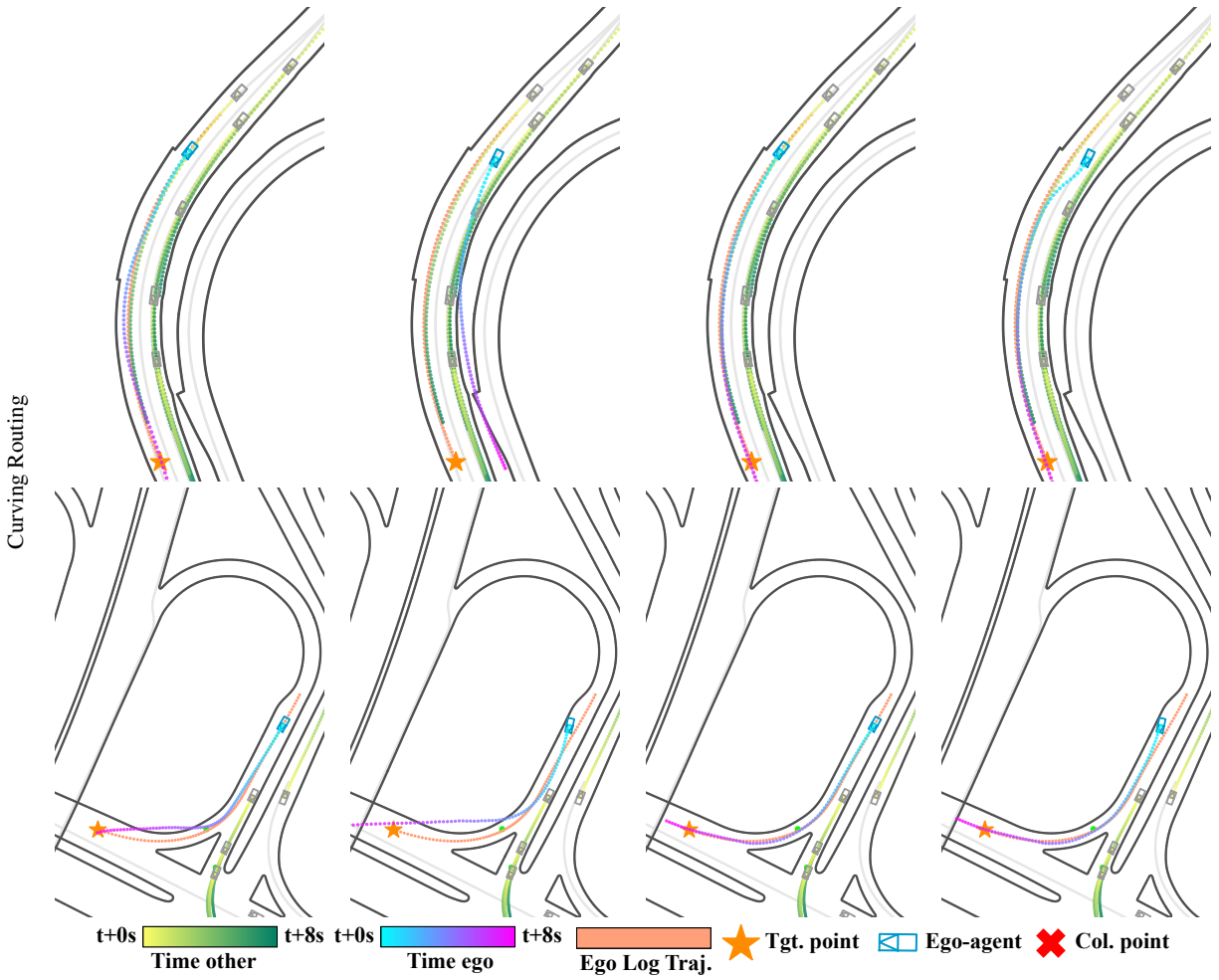


Figure 11: Visualisation of *close-loop* evaluation on dual carriageways. The imagery in the first row illustrates a section of motorways that is both curvaceous and narrow. The last row is dedicated to showcasing a slip road facilitating exit the dual carriageways. Notably, from the depiction in the two examples, there is an observable increase in curvature.

